

Silicon-photonic optomechanical magnetometer

Fernando Gottardo^{1,2}, Benjamin J. Carey^{1,2,3},
Nathaniel Bawden^{1,2,3}, Glen I. Harris^{1,2}, Hamish Greenall^{1,2},
Erick Romero^{1,2}, Douglas Bulla⁴, James S. Bennett^{5,6},
Scott Foster⁴, Warwick P. Bowen^{1,2,3*}

¹School of Mathematics and Physics, The University of Queensland, St Lucia, 4067, Queensland, Australia.

²ARC Centre of Excellence for Engineered Quantum Systems, St Lucia, 4067, Queensland, Australia.

³ARC Centre of Excellence in Quantum Biotechnology, St Lucia, 4067, Queensland, Australia.

⁴Australian Government Department of Defence Science and Technology, Edinburgh, 5111, South Australia, Australia.

⁵Centre for Quantum Dynamics, Griffith University, Nathan, 4111, Queensland, Australia.

⁶School of Mathematical Sciences, Queensland University of Technology, Gardens Point, 4000, Queensland, Australia.

*Corresponding author(s). E-mail(s): w.bowen@uq.edu.au;

Abstract

Optomechanical sensors enable exquisitely sensitive force measurements, with emerging applications across quantum technologies, standards, fundamental science, and engineering. Magnetometry is among the most promising applications, where chip-scale optomechanical sensors offer high sensitivity without the cryogenics or magnetic shielding required by competing technologies. However, lack of compatibility with integrated photonics and electronics has posed a major barrier. Here we introduce silicon-on-insulator optomechanical magnetometers to address this barrier. A new post-release lithography process enables high-quality metallisation of released mechanical structures, overcoming the incompatibility between silicon-on-insulator fabrication and functional magnetic films. This allows us to employ photonic-crystal cavities that enhance motion-to-optical signal transduction by over an order of magnitude. The resulting devices achieve magnetic field sensitivity of $800 \text{ pT}/\sqrt{\text{Hz}}$, three orders of magnitude beyond

previous waveguide-integrated designs. The advances we report provide a path towards high-performance, room temperature and chip-integrated magnetometers for applications ranging from biomedical imaging and navigation to resource exploration.

Keywords: Optomechanical sensing, Magnetometry, Silicon-Photonics, Microfabrication, On-chip optomechanics, On-chip Magnetometer

Originally pioneered to enable gravitational wave detection [1], optomechanical sensors harness optical and mechanical resonances to achieve exquisitely sensitive measurements [2]. Recent years have seen a rapid acceleration in chip-scale optomechanical sensing, driven by applications in quantum computation and communications [3], and in fundamental science such as dark matter detection [4, 5] and the foundations of quantum mechanics [6]. These sensors are now able to measure forces and displacements with attonewton [7, 8] and attometre [9] sensitivity, respectively, and allow ultrasound and acceleration measurements with otherwise inaccessible precision [10–12]. They are even able to resolve quantum zero-point motion [13], and have enabled a new class of quantum-calibrated temperature standards [14].

Magnetometry is a particularly important application area, with potential impact across medical imaging [15–17], navigation [18, 19], chemical analysis [20, 21], and geological surveying [22–24]. Unlike other precision magnetometers [25, 26], optomechanical magnetometers require no cryogenics or magnetic shielding [27, 28], providing high magnetic field sensitivity at room temperature and in background fields as large as that of the Earth [18]. Recent advances have reached hundreds-of-femtotesla [29] sensitivity, with sensitivity now rivaling that of state-of-the-art cryogenic magnetometers of similar size [22, 30, 31]. However, previous optomechanical magnetometers [27, 28, 30–33] have had limited compatibility with integrated photonics or electronics, constraining both performance and applicability. We overcome this barrier, developing an optomechanical magnetometer based on silicon-on-insulator (SOI), an industry-standard for scalable photonic integration [34, 35].

Previous work has found that standard SOI fabrication processes degrade functional metallic films [36], such as those used in optomechanical magnetometers [31, 33]. We address this significant challenge, developing a new post-release lithography technique which enables high-quality metallisation of delicate mechanical elements and is readily transferable to other microsystems requiring functional films on released structures, such as MEMs magnetometers [37, 38], magnetoelectric and magnetoacoustic transducers [39, 40], spin-filters [41], bolometers [42, 43], and quantum information devices [44, 45].

The use of post-release lithography allows us to create complex functional devices on SOI. Going beyond previous whispering-gallery-based optomechanical magnetometers [27, 28, 30–33], it allows optomechanical magnetometers that co-integrate magneto-mechanical and photonic structures, independently optimized for magnetic coupling and optical readout, and with photonic crystal resonators for readout. This

increases the transfer of magnetic-field-induced motion into optical signal by a factor of 27. The resulting sensor achieves a peak sensitivity of $800 \text{ pT}/\sqrt{\text{Hz}}$, more than three orders of magnitude better than previous waveguide-integrated devices [33].

Together, these advances pave the way for scalable chip-scale optomechanical magnetometers with potential applications ranging from biomedical imaging to geological surveying.

1 Fabricating functional suspended devices on silicon-on-insulator

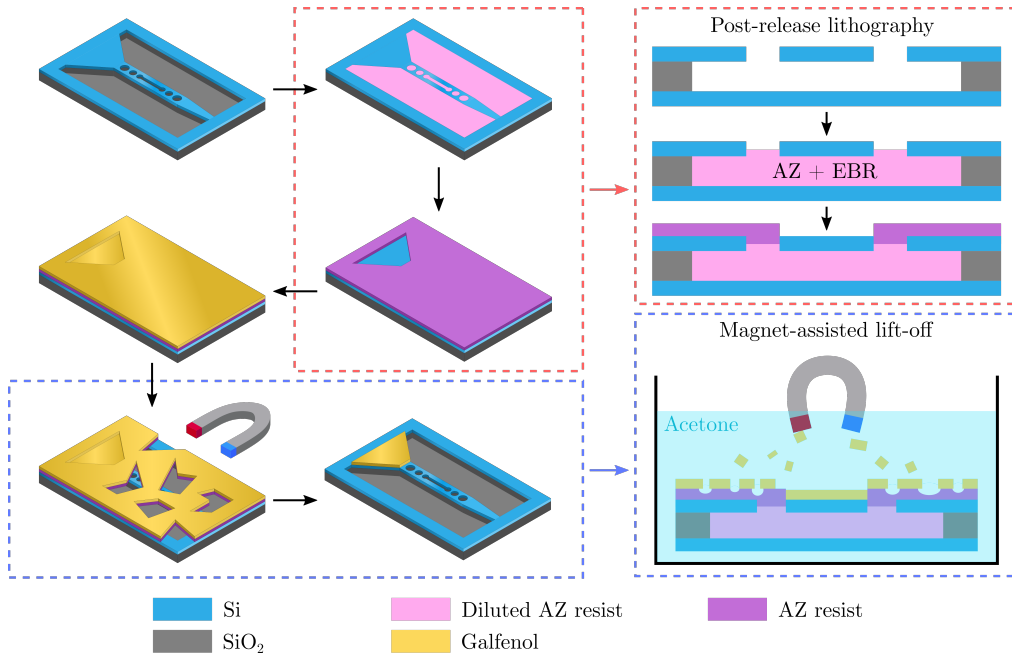


Fig. 1 Overview of the post-release fabrication process. A freestanding optomechanical device is flooded with diluted resist solution (AZ + EBR) prior to photolithography and galfenol deposition. The excess galfenol and structure supporting resist are removed via a magnetically-assisted lift-off process, followed by critical point drying, resulting in the final device.

Optomechanical magnetometers function by detecting minute motions caused by magnetic-field-induced stress, or magnetostriction [27]. They achieve high sensitivity by using optical cavities to precisely measure the magnetostrictive response of compliant suspended structures, whose motion is enhanced by mechanical resonances [2]. All previous on-chip optomechanical magnetometers have used a silica device layer [27, 28, 30–33]. This has significant advantages; providing access to ultrahigh quality optical resonances [46, 47] and allowing gentle, selective release of

fragile suspended structures via xenon difluoride vapor phase etching [48, 49]. However, silica’s low refractive index limits compatibility with integrated electronics and photonics, and makes it difficult to engineer complex and compact structures [50]. Indeed, all previous on-chip optomechanical magnetometers have employed simple circular whispering gallery mode cavities [27, 28, 30–33], with far weaker signal transduction from mechanical to optical domains than can be achieved in more complex devices [51, 52].

To enable full integration and provide access to the rich spectrum of optomechanical device architectures that have developed in recent years [53–59], it is necessary to translate optomechanical magnetometry onto a higher refractive index device layer. Silicon-on-insulator (SOI) – consisting of a silicon device layer atop a silica sacrificial layer – is particularly attractive, since it is a primary industry standard for photonic integration [60, 61]. To release functional devices, it is necessary to under-etch the sacrificial layer. In SOI, this generally requires vapor phase hydrofluoric acid etching [62], which is known to degrade a range of metal alloys [36]. We attempted vapor phase hydrofluoric acid etching of devices coated with the magnetostrictive material, galfenol ($\text{Fe}_{81}\text{Ga}_{19}$) [63–65]. Even with a protective tantalum capping layer, fluorine penetration during etching eliminated any measurable response (see Sec. S.1). An aluminium capping layer was also tested, but did not exhibit a magnetic response due to HF attacking the galfenol through the exposed sidewall. The galfenol could potentially be fully encapsulated using a second lithography step to define a region slightly larger than the galfenol and depositing an appropriately thick aluminium layer. However, this would restrict the sensors motion, and add a second round of lithography, deposition, and liftoff.

To remove degradation from the release step, we developed a new post-release lithography and deposition process that is robust and broadly generalisable (Fig. 1). In the usual fabrication process, because of the extreme fragility of the suspended structures, the release step is performed last – after deposition of the magnetostrictive material, and exposing it to risk of degradation [2]. Our new process flips this order, depositing the magnetostrictive material *after* release. This means that the thin-film is deposited at the end of the process, avoiding any deleterious effects from the other fabrication steps. The major challenge then is to protect the fragile released structures during lithography and deposition. This hurdle is specific to technologies that require thin device layers – in our case hundreds of nanometers thick, to support single-mode silicon photonics [35]. In contrast, MEMs typically utilise a much thicker device layer, up to $10\ \mu\text{m}$ [66], greatly increasing robustness and resilience to subsequent fabrication procedures.

A critical step to achieve post-release lithography was the development of a method to support the released devices, embedding them in partially solidified photoresist (Fig. 1). For this step, the photoresist was diluted with edge bead removal solvent to reduce its viscosity and allow gentle spin coating at a low speed of 1000 RPM. With an empirically determined dilution ratio of equal parts photoresist and solvent, we found that this process did not harm the released structures, provided sufficient support during the subsequent fabrication procedures, and allowed easy removal during

the final liftoff of the excess magnetostrictive material. Attempts using undiluted photoresist, with its relatively high viscosity and requiring typical spin coating speeds, broke the structures.

The fabrication process, in brief, is as follows (see Methods for full details): an SOI chip, comprising a silicon device layer of 215 nm approximate thickness atop a 3 μm thick sacrificial silica layer, is patterned using electron beam lithography (EBL) and etched with reactive ion etching. The devices are then released using HF vapor phase etching. After release, a low-viscosity resist is spin-coated to fill the etched regions and support the suspended elements. This support layer is cured and reinforced with a second coating, allowing standard photolithography to define the galfenol deposition area without collapsing the devices (Fig. 1). A 600 nm galfenol layer is then deposited by DC sputtering.

Following deposition, excess galfenol is removed via a lift-off process. However, typical lift-off processes involving sonication in solvent were found to damage the released structures. To address this, we devised an alternative, magnetically assisted lift-off process (Fig. 1). Here, the chip is submerged in acetone and a neodymium permanent magnet is placed approximately 5 mm above. This magnet promotes the removal of galfenol and prevents redeposition on the chip. At the same time, the acetone removes the semi-solidified resist supporting the structure. The chips are then dried with critical-point carbon dioxide.

We characterised the magnetostrictive properties of the galfenol films after the fabrication process using optical profilometry [65]. In contrast to the conventional method, where no response was observed, the films were found to present piezomagnetic stress and strain coupling coefficients of $\alpha_{33} = 2 \times 10^8 \text{ Pa/T}$ and $d_{33} = 3.2 \text{ nm/A}$, respectively (these values were used in the modeling shown in Fig. 4d and Sec. S.3.3). The piezomagnetic coefficients of the thin film determine the efficacy of transduction of magnetic fields to mechanical motion via applied stress and strain, respectively. The measured values are comparable to other thin-film galfenol measurements [65, 67, 68], with the highest reported strain coupling coefficient being 16 nm/A [68].

2 Optomechanical magnetometry on silicon-on-insulator

The availability of post-release lithography and deposition allowed fabrication of optomechanical magnetometers on SOI, exploiting the high refractive index silicon device layer to enable complex designs. The magnetometer design is shown in Fig. 2, along with a scanning electron micrograph of a fabricated device. The magnetometers consist of a photonic crystal cavity, connected to a separate magnetostrictive actuator as well as an on-chip waveguide for optical excitation and read-out. Light is coupled to and from the waveguide using a single-sided tapered fiber, which can be bonded to the waveguide using ultraviolet-curing adhesive [69] (See Section S.2).

The physical separation of cavity and magnetic actuator allows each to be independently optimised. The actuator consists of a triangular mechanical cantilever with an out-of-plane mechanical ‘flapping mode’ resonance that is coated with a film of

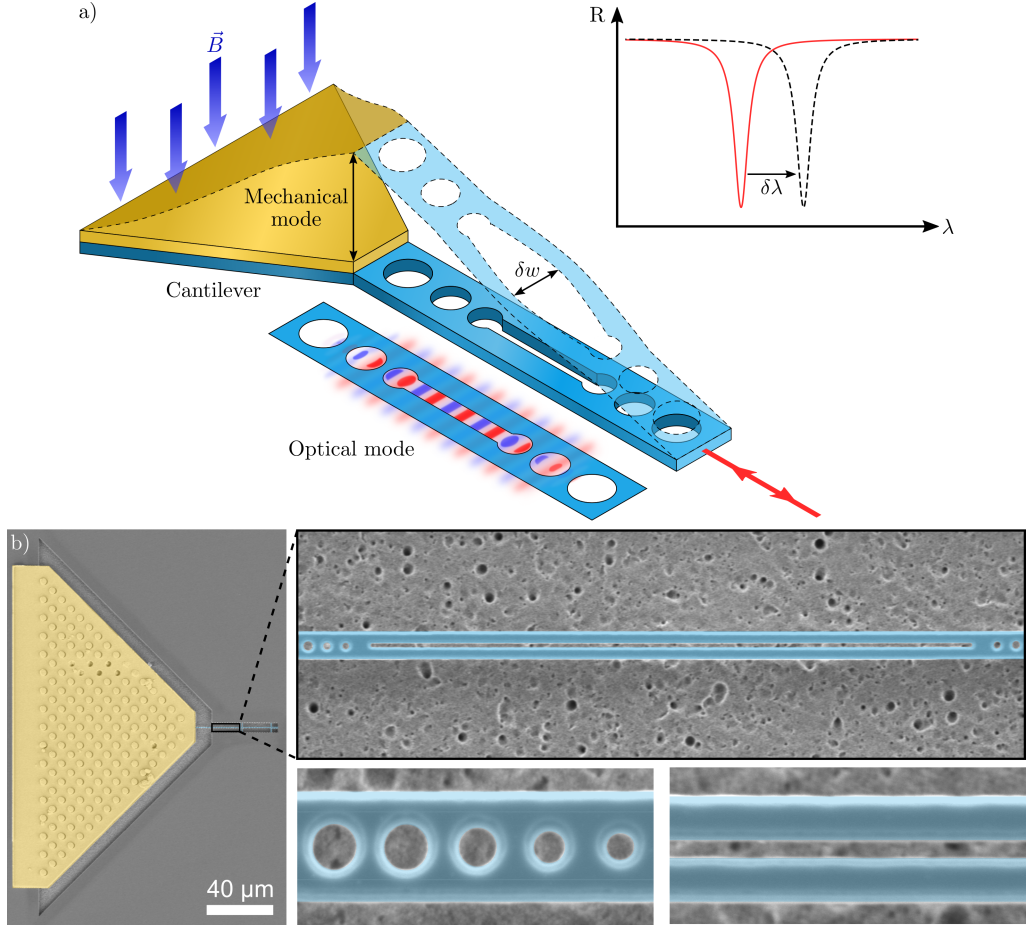


Fig. 2 a) Schematic diagram of the device design and working principle. A magnetic field (\vec{B}) induces deformation of a galfenol (yellow) platform, which pulls on a silicon (blue) slot cavity. The resulting in-plane deformation of the cavity (δw) induces a change in its optical resonance wavelength ($\delta\lambda$). This can be detected by probing the reflected light. The red arrows indicate coupling of the optical mode to an on-chip waveguide. b) False color SEM image of a magnetometer with close-up images of the slot cavity. Silicon, blue; galfenol, yellow.

galfenol. Applying a magnetic field produces strain within the galfenol film, which in turn drives mechanical motion of the cantilever. The tip of the cantilever is connected to one end of the photonic crystal cavity, facilitating the conversion of mechanical motion into measurable optical frequency shifts.

The photonic crystal cavity is defined by a silicon waveguide with photonic crystal (PhC) mirrors at either end [70]. We etch a slot along the center of the waveguide. This introduces a set of gap-modes [71], the optical fields of which are strongly concentrated within the slot (Fig. 3b). The resonance frequencies of these modes are

exquisitely sensitive to changes in the slot width, amplifying the effect of mechanical motion on the optical resonance frequency. Moreover, the presence of the slot greatly increases the compliance of the cavity, increasing the mechanical displacements induced by magnetostrictive forces. Together, this significantly enhances the conversion from magnetic field to optical signal.

We use Finite Element Method (FEM) modeling (COMSOL Multiphysics) to optimise the design of the magnetometer. Fig. 3a depicts the fundamental mechanical mode of the magnetic actuator, with a resonance frequency of 250 kHz. It is apparent that the displacement of the actuator is primarily out of plane. However, this causes an elongation of the highly mechanically compliant photonic cavity, which in turn drives a change in the slot width. The optical eigenmode of the slot cavity is depicted in Fig. 3b. This confirms that the majority of the electric field is tightly confined within the air gap of the slot.

Employing a longer slot amplifies the change in slot width due to applied magnetic fields by the increased mechanical compliance. However, it also increases the slots thermomechanical motion, obscuring the motion of the galphenol cantilever and reducing sensitivity. The transfer efficiency from cantilever motion to slot motion must therefore be balanced against slot thermomechanical noise to optimise sensitivity. We found that a 7 μm slot length to be suitable for this purpose. The conversion of mechanical motion to optical frequency shift is quantified by the optomechanical coupling rate, $G_{\text{OM}} = \partial\omega/\partial x$, where x is the slot width. We modeled this dependency for our slotted photonic crystal designs (Sec. S.3.1), finding that the optomechanical coupling rate increases as the width of the slot decreases, and eventually rolls off at small slot widths. We chose a width of 100 nm, providing a high optomechanical coupling rate, while also allowing reliable fabrication without risk of the slot collapsing or not being fully released. This separation yields a coupling rate of 99.8 GHz/nm, comparable to the highest reported for optomechanical cavities [52, 72–74] and a factor of twenty-seven higher than the best previous chip-scale optomechanical magnetometers [31].

3 Waveguide-integrated magnetometer with sub-nanotesla sensitivity

We assess the performance of the fabricated magnetometer using the experimental configuration illustrated in Figure 4a). Here, light from a tunable laser (EXFO T100S-HP, 1500-1600 nm) is coupled from a single-sided tapered optical fiber into the device’s inverted tapered waveguide, in a similar manner to that presented in [75, 76]. The reflected light is then directed to a photodetector (New Focus 1811) with the aid of a circulator (the detected optical power was approximately 1 μW). Monitoring the photodiode output while sweeping the laser wavelength reveals the optical resonance of the slot cavity, shown in Fig. 4b). Fitting a Lorentzian lineshape to the reflected spectrum gives the cavity energy loss rate $\kappa/2\pi = 205 \text{ GHz}$ and an optical quality factor ($Q_o = \omega_o/\kappa$) of $\sim 10^3$. These are comparable to previously reported slotted photonic crystal cavities in SOI [77–79].

In order to determine the magnetic field sensitivity, the laser wavelength was tuned to the side of the optical resonance and the photodiode output was monitored by

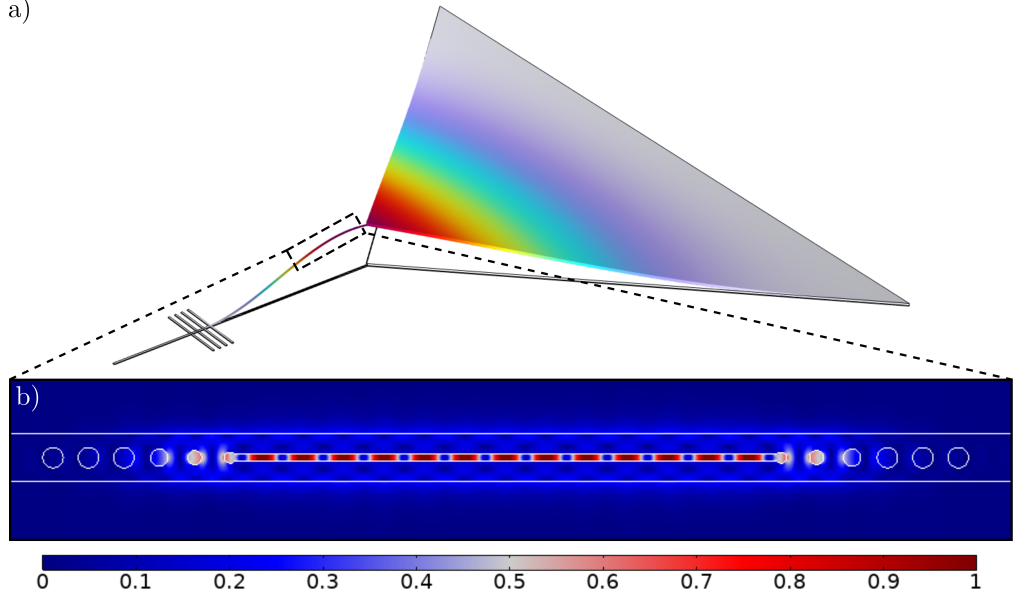


Fig. 3 Finite element method modeling with COMSOL. a) Modeshape of the fundamental out-of-plane vibrational mode. b) Intensity distribution of the 1D photonic slot cavity's optical mode (normalised by the peak intensity).

network and spectrum analysers (Liquid Instruments Moku:Pro). In this configuration, changes to the optical resonance frequency produce amplitude modulations of the reflected light. Gas damping reduces the mechanical quality factor of the galfeinol coated cantilever, and hence the overall sensitivity of our magnetometer. To improve performance, the device and the driving coil were placed in a vacuum chamber and sensitivity measurements were performed at a pressure of 1×10^{-3} mbar (see Supp. Sec. S.4 for comparison to atmospheric pressure). This is a relatively modest vacuum, compatible with chip-scale vacuum packaging capabilities [80]. In the absence of a magnetic driving field, a broad mechanical resonance was observed, with a quality factor of $Q = 635$. The peak frequency agreed with that of the eigenmode found using the FEM analysis discussed in Sec. 2.

An AC magnetic field was generated by driving a home-made copper coil with a $10 V_{pp}$ sinusoidal signal, delivering a 410 nT RMS AC field at the device. The sensitivity at this frequency (ω_{ref}) is determined from the measured signal-to-noise ratio ($SNR = S(\omega_{ref})/N(\omega_{ref})$) of the response to this drive by [28]:

$$B_{min}(\omega_{ref}) = \frac{B_{AC}}{\sqrt{SNR \times RBW}}, \quad (1)$$

where RBW is the spectrum analyzer resolution bandwidth and B_{AC} is the applied magnetic field. Eq. (1) can be used in conjunction with the network response of the system to determine the sensitivity spectrum of the device ($B_{min}(\omega)$) by [28]:

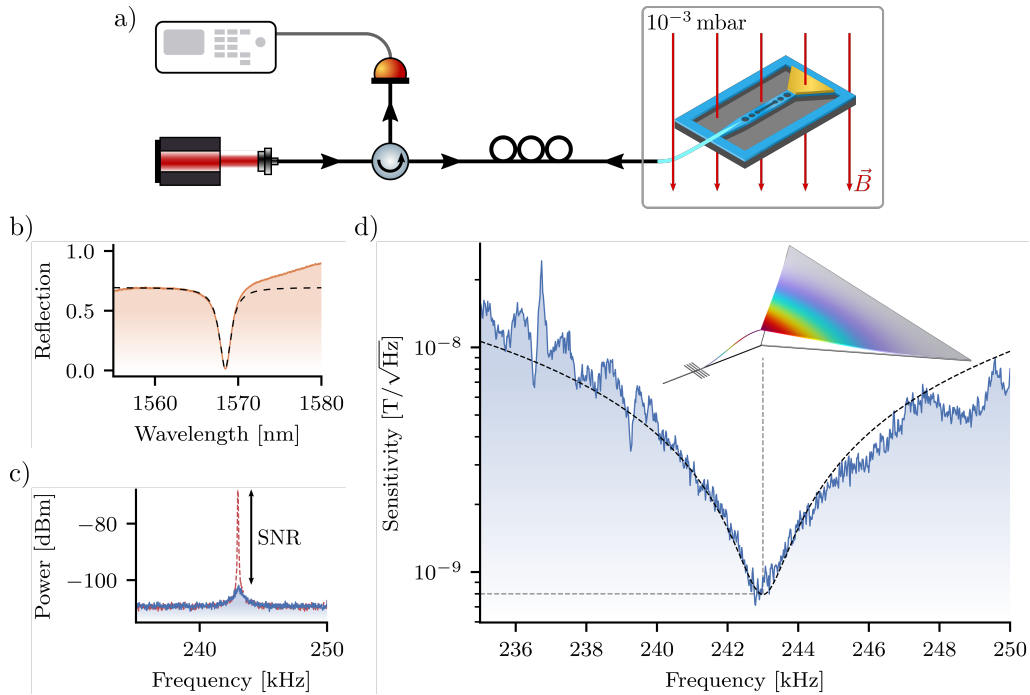


Fig. 4 Magnetometer characterization. a) Experimental setup for sensitivity measurements. b) Optical spectrum reflected from the slot cavity. The Lorentzian fit (dashed) gives an optical quality factor of 930. c) Power spectrum showing the mechanical mode and the signal from an applied field measured with a 30 Hz RBW. d) Sensitivity spectrum around the mechanical resonance. The black dashed line shows the sensitivity calculated from the thermomechanical noise model using the relevant parameter derived both experimentally and from the FEM model

$$B_{\min}(\omega) = \sqrt{\frac{S(\omega_{\text{ref}})}{S(\omega)} \frac{N(\omega)}{N(\omega_{\text{ref}})}} \times B_{\min}(\omega_{\text{ref}}), \quad (2)$$

where $S(\omega)$ is the signal measured by the network analyzer and $N(\omega)$ is the noise floor measured with the frequency spectrum analyzer [27]. The resulting sensitivity spectrum is shown in Fig. 4d). The high optomechanical coupling suppressed the optical noise well below the thermomechanical noise due to the random thermally-driven motion of the slot and cantilever, with the modelled thermomechanical noise limit (see Sec. S3.3), agreeing well with measurements (dashed black curve, Fig. 4d). A peak sensitivity of 800 pT/ $\sqrt{\text{Hz}}$ is observed at a frequency of 243 kHz, corresponding to the mechanical resonance of the cantilever. This sensitivity is an improvement of several orders of magnitude when compared to previous on-chip waveguide-integrated optical magnetometers [33, 81, 82].

4 Discussion

The transition to a silicon-on-insulator (SOI) platform reported here represents a key enabler for chip-scale optomechanical magnetometry. Beyond its compatibility with photonic and electronic integration [61], SOI supports high-yield fabrication of suspended mechanical structures with submicron precision using standard lithographic tools [83]. This opens a viable path to monolithically integrated systems that combine optical readout, magnetic transduction, and CMOS-compatible control circuitry – a level of integration that is not achievable with previous approaches. Previous optomechanical magnetometers have achieved peak sensitivity only within narrow frequency bands near mechanical resonances, with optical noise dominating across the rest of the spectrum. This significantly constrains possible applications, as most real-world use cases – including navigation, magnetoencephalography, and geophysical surveying – require operation at frequencies well below the mechanical resonance [2].

By greatly increasing the optomechanical coupling strength, and thereby suppressing optical noise, our devices represent a significant step toward resolving this challenge. Although our sensors also exhibit peak sensitivity near resonance, the limiting factor is now thermomechanical noise rather than optical readout. Optical noise is typically dominated by shot noise near resonance and exhibits hard-to-suppress $1/f$ -like behaviour at low frequencies [84]. By comparison, thermomechanical noise can be more readily mitigated through structural optimisation [57]. In our devices, the dominant near-resonance noise arises from thermomechanical fluctuations of the galfenol-coated cantilever. This can be reduced by increasing the mechanical quality factor and by improving the transduction of magnetostrictive strain into transverse motion. The mechanical quality factor of the cantilever is not optimised, and is many orders-of-magnitude below the state-of-the-art – now approaching 10^8 at room temperature [57]. It is constrained primarily by clamping losses, which can be greatly suppressed using soft clamping techniques that are enabled by the transition to SOI [54].

Away from resonance, the thermomechanical noise is dominated by motion of the slotted photonic crystal cavity. This is due to the presence of confined mechanical resonances that coexist with the desired confined optical mode. These high frequency resonances are strongly coupled to the optical mode. While the noise from the galfenol-coated cantilever has the same Lorentzian frequency dependence as the response to magnetic signals, and would result in a flat broadband magnetic sensitivity if fully dominant [85], the photonic crystal noise is effectively white across our full detection band. This results in degraded sensitivity away from the cantilever resonance frequency. Photonic crystal thermomechanical noise could be greatly reduced by designing the crystal to not support confined mechanical resonances [86], or to suppress their motional amplitudes [87]. Its contribution to the measured signal could be further reduced by increasing the mechanical coupling between the cantilever and the slot structure.

Further, increasing the piezomagnetic coefficients (α_{33} & d_{33}) would proportionally improve the sensitivity of the magnetometer across the full frequency band. As discussed in Sec. 1, improved galfenol thin films could allow a factor of four increase in these parameters [68]. Recent reports of other magnetostrictive materials such as

galfenol-B (FeGaB) thin films have demonstrated even higher values of d_{33} , as high as 150 nm/A [88]. Employing such materials could improve the sensitivity by a factor over 45 to around 17 pT/ $\sqrt{\text{Hz}}$. Together, these strategies provide a feasible route to both improve the sensitivity to below 100 fT/ $\sqrt{\text{Hz}}$ and extend high-sensitivity operation beyond narrow resonant bands, in a microscale, integrated magnetometer with microwatt optical power requirements. Further improved sensitivity could be achieved by increasing the device footprint to allow for a larger magnetostrictive element.

Our devices are already substantially more sensitive than previous waveguide-integrated optomechanical magnetometers, but are several orders of magnitude less sensitive than the best non-waveguide-integrated devices. We expect this sensitivity deficit to be overcome via the engineering strategies and material optimization discussed above. Ultimately, optomechanical magnetometers may provide a compelling alternative to SQUIDs, OPMs, and fluxgate sensors – offering comparable performance with dramatically lower size, weight, power, and cost.

5 Methods

5.1 Fabrication details

A silicon-on-insulator wafer (750 μm Si/3 μm SiO₂/0.22 μm Si) was cleaned and spin-coated with a 350 nm layer of electron-beam resist (ARP 6200.09). The device structure was defined using electron beam lithography (Raith EBPG 5150, 260 $\mu\text{C}/\text{cm}^2$ dose) and developed with AR 600-546 (All Resist) then rinsed with o-Xylene and isopropyl alcohol (IPA). The exposed silicon was etched by reactive ion-etching (Oxford Instruments PlasmaPro NGP80, 50 sccm SF₆ & 100 sccm CHF₃ at 82 W RF power) forming the optical structures and cantilever in the Si device layer atop the buried oxide (BOX) silica layer. The devices were then cleaned before being released with hydrofluoric acid (HF) vapor phase etching (VPE) at 35°C for 15 minutes. To enable complete release of the large triangular cantilevers (200 μm base \times 100 μm height), holes were added to allow the HF vapor to reach the silica underneath.

Photoresist (AZ nLoF 2020) was diluted in equal parts with edge bead removal (EBR) solvent to significantly reduce its viscosity. This diluted photoresist solution was spin-coated onto the released devices at a speed of 1000 RPM, removing the solution from the top of the device layer while filling the volume of the removed BOX. This was followed by baking at 100°C for 60s to partially solidify the solution. The procedure was then repeated to ensure complete substitution of the removed BOX and provide a supporting layer underneath the released devices. The galfenol deposition area was then defined by patterning with a typical photolithography method by spin-coating undiluted AZ nLoF 2020, photolithographic exposure (MLA150, Heidelberg Instruments Maskless aligner), and development in AZ 726. The magnetostrictive thin-film was then deposited by DC sputtering (Temescal FC-2000) a 5 nm tantalum adhesion layer, 16 nm copper seeding layer, 600 nm galfenol layer, and a 5 nm tantalum capping layer to protect against oxidation. Excess galfenol was removed in acetone via a magnetically assisted liftoff process. The fabrication process was completed by transferring the chip with freestanding devices into IPA followed by carbon dioxide critical point drying (Leica EM 300CPD) to eliminate stiction.

Supplementary information. See Supplemental Material for supporting content, including additional information on fabrication procedures, investigations of the effects of HF on galfenol, fiber bonding to the integrated waveguide, further modeling of the device and the thermomechanical limited sensitivity, and details of mechanical modes with varying pressure.

Acknowledgements. The authors acknowledge the facilities, and the scientific and technical assistance, of the Australian Microscopy & Microanalysis Research Facility at the Centre for Microscopy and Microanalysis, The University of Queensland. This work was performed in part at the Queensland node of the Australian National Fabrication Facility, a company established under the National Collaborative Research Infrastructure Strategy to provide nano- and microfabrication facilities for Australia’s researchers. The Commonwealth of Australia (represented by the Defence Science and Technology Group) supports this research through a Defence Science Partnerships agreement. This work was funded under the NGTF and is being delivered through the ASCA. This work was financially supported by the Australian Research Council (ARC) Centres of excellence for Engineered Quantum systems (EQUS, Grant No. CE170100009) and Quantum Biotechnology (Grant No. CE230100021). We thank the Queensland Defence Science Alliance (QDSA) for financial support of the project through the 2023 QDSA Collaborative Research Grant (CRG) funding round. The authors acknowledge the highly valuable advice and support provided by Rodney Appleby and financial support by Orica Australia *Pty Ltd*. This project was funded by the Queensland Government through the Department of Environment, Tourism, Science and Innovation’s (DETSI) Quantum 2032 Challenge Program. The program accelerates quantum sportstech, connects Queensland’s research sector with industry, and showcases the state’s quantum capabilities as part of Brisbane 2032’s legacy.

Declarations

The authors declare no conflicts of interest.

References

- [1] Abramovici, A., Althouse, W.E., Drever, R.W., Gürsel, Y., Kawamura, S., Raab, F.J., Shoemaker, D., Sievers, L., Spero, R.E., Thorne, K.S., *et al.*: LIGO: The laser interferometer gravitational-wave observatory. *science* **256**(5055), 325–333 (1992)
- [2] Li, B.-B., Ou, L., Lei, Y., Liu, Y.-C.: Cavity optomechanical sensing. *Nanophotonics* **10**(11), 2799–2832 (2021)
- [3] Barzanjeh, S., Xuereb, A., Gröblacher, S., Paternostro, M., Regal, C.A., Weig, E.M.: Optomechanics for quantum technologies. *Nature Physics* **18**(1), 15–24 (2022)

- [4] Brady, A.J., Chen, X., Xia, Y., Manley, J., Dey Chowdhury, M., Xiao, K., Liu, Z., Harnik, R., Wilson, D.J., Zhang, Z., *et al.*: Entanglement-enhanced optomechanical sensor array with application to dark matter searches. *Communications Physics* **6**(1), 237 (2023)
- [5] Baker, C.G., Bowen, W.P., Cox, P., Dolan, M.J., Goryachev, M., Harris, G.: Optomechanical dark matter instrument for direct detection. *Physical Review D* **110**(4), 043005 (2024)
- [6] Aspelmeyer, M., Kippenberg, T.J., Marquardt, F.: Cavity optomechanics. *Reviews of Modern Physics* **86**(4), 1391–1452 (2014)
- [7] Gavartin, E., Verlot, P., Kippenberg, T.J.: A hybrid on-chip optomechanical transducer for ultrasensitive force measurements. *Nature nanotechnology* **7**(8), 509–514 (2012)
- [8] Mason, D., Chen, J., Rossi, M., Tsaturyan, Y., Schliesser, A.: Continuous force and displacement measurement below the standard quantum limit. *Nature Physics* **15**(8), 745–749 (2019)
- [9] Schliesser, A., Anetsberger, G., Rivière, R., Arcizet, O., Kippenberg, T.J.: High-sensitivity monitoring of micromechanical vibration using optical whispering gallery mode resonators. *New Journal of Physics* **10**(9), 095015 (2008)
- [10] Basiri-Esfahani, S., Armin, A., Forstner, S., Bowen, W.P.: Precision ultrasound sensing on a chip. *Nature Communications* **10**(1), 132 (2019)
- [11] Cao, X., Yang, H., Wang, M., Hu, Z.-G., Wu, Z.-L., Wang, Y., Liu, J.-F., Zhou, X., Li, J., Lao, C., *et al.*: Integrated optomechanical ultrasonic sensors with nanopascal-level sensitivity. *arXiv preprint arXiv:2506.20219* (2025)
- [12] Bawden, N., Carey, B.J., Yeo, P.-M., Arora, N., Sementilli, L., Valenzuela, V.M., Romero, E., Harris, G.I., Wegener, M., Bowen, W.P.: Precision optomechanical accelerometer via hybrid test mass integration. *arXiv preprint arXiv:2508.16088* (2025)
- [13] Huang, G., Beccari, A., Engelsens, N.J., Kippenberg, T.J.: Room-temperature quantum optomechanics using an ultralow noise cavity. *Nature* **626**(7999), 512–516 (2024)
- [14] Purdy, T.P., Grutter, K.E., Srinivasan, K., Taylor, J.M.: Quantum correlations from a room-temperature optomechanical cavity. *Science* **356**(6344), 1265–1268 (2017)
- [15] Brookes, M.J., Leggett, J., Rea, M., Hill, R.M., Holmes, N., Boto, E., Bowtell, R.: Magnetoencephalography with optically pumped magnetometers (OPM-MEG): the next generation of functional neuroimaging. *Trends in Neurosciences* **45**(8),

621–634 (2022)

- [16] Murzin, D., Mapps, D.J., Levada, K., Belyaev, V., Omelyanchik, A., Panina, L., Rodionova, V.: Ultrasensitive magnetic field sensors for biomedical applications. *Sensors* **20**(6), 1569 (2020)
- [17] Borna, A., Carter, T.R., Colombo, A.P., Jau, Y.-Y., McKay, J., Weisend, M., Taulu, S., Stephen, J.M., Schwindt, P.D.: Non-invasive functional-brain-imaging with an OPM-based magnetoencephalography system. *Plos one* **15**(1), 0227684 (2020)
- [18] Bennett, J.S., Vyhnalek, B.E., Greenall, H., Bridge, E.M., Gotardo, F., Forstner, S., Harris, G.I., Miranda, F.A., Bowen, W.P.: Precision magnetometers for aerospace applications: A review. *Sensors* **21**(16) (2021)
- [19] Connerney, J., Espley, J., Lawton, P., Murphy, S., Odom, J., Oliverson, R., Sheppard, D.: The MAVEN magnetic field investigation. *Space Science Reviews* **195**(1), 257–291 (2015)
- [20] Savukov, I., Romalis, M.V.: Nmr detection with an atomic magnetometer. *Physical Review Letters* **94**(12), 123001 (2005)
- [21] DeVience, S.J., Pham, L.M., Lovchinsky, I., Sushkov, A.O., Bar-Gill, N., Belthangady, C., Casola, F., Corbett, M., Zhang, H., Lukin, M., *et al.*: Nanoscale nmr spectroscopy and imaging of multiple nuclear species. *Nature nanotechnology* **10**(2), 129–134 (2015)
- [22] Stolz, R., Schiffler, M., Becken, M., Thiede, A., Schneider, M., Chubak, G., Marsden, P., Bergshjorth, A.B., Schaefer, M., Terblanche, O.: Squids for magnetic and electromagnetic methods in mineral exploration. *Mineral Economics* **35**(3), 467–494 (2022)
- [23] Lu, Y., Zhao, T., Zhu, W., Liu, L., Zhuang, X., Fang, G., Zhang, X.: Recent progress of atomic magnetometers for geomagnetic applications. *Sensors* **23**(11), 5318 (2023)
- [24] Stele, A., Kaub, L., Linck, R., Schikorra, M., Fassbinder, J.W.: Drone-based magnetometer prospection for archaeology. *Journal of Archaeological Science* **158**, 105818 (2023)
- [25] Storm, J.-H., Hömmen, P., Drung, D., Körber, R.: An ultra-sensitive and wide-band magnetometer based on a superconducting quantum interference device. *Applied Physics Letters* **110**(7) (2017)
- [26] Savukov, I., Karaulanov, T.: Magnetic-resonance imaging of the human brain with an atomic magnetometer. *Appl. Phys. Lett.* **103**(4) (2013)

- [27] Forstner, S., Prams, S., Knittel, J., Ooijen, E.D., Swaim, J.D., Harris, G.I., Szorkovszky, A., Bowen, W.P., Rubinsztein-Dunlop, H.: Cavity optomechanical magnetometer. *Phys. Rev. Lett.* **108**, 120801 (2012)
- [28] Forstner, S., Sheridan, E., Knittel, J., Humphreys, C.L., Brawley, G.A., Rubinsztein-Dunlop, H., Bowen, W.P.: Ultrasensitive optomechanical magnetometry. *Adv. Mater.* **26**(36), 6348–6353 (2014)
- [29] Xu, A.-N., Li, Y., Li, X., Liu, B., Liu, Y.-C.: Subpicotesla optomechanical magnetometry. *Physical Review Letters* **133**(15), 153601 (2024)
- [30] Li, B.-B., Brawley, G., Greenall, H., Forstner, S., Sheridan, E., Rubinsztein-Dunlop, H., Bowen, W.P.: Ultrabroadband and sensitive cavity optomechanical magnetometry. *Photon. Res.* **8**(7), 1064–1071 (2020)
- [31] Hu, Z.-G., Gao, Y.-M., Liu, J.-F., Yang, H., Wang, M., Lei, Y., Zhou, X., Li, J., Cao, X., Liang, J., *et al.*: Picotesla-sensitivity microcavity optomechanical magnetometry. *Light: Science & Applications* **13**(1), 279 (2024)
- [32] Li, B.-B., Bílek, J., Hoff, U.B., Madsen, L.S., Forstner, S., Prakash, V., Schäfermeier, C., Gehring, T., Bowen, W.P., Andersen, U.L.: Quantum enhanced optomechanical magnetometry. *Optica* **5**(7), 850–856 (2018)
- [33] Gotardo, F., Carey, B.J., Greenall, H., Harris, G.I., Romero, E., Bulla, D., Bridge, E.M., Bennett, J.S., Foster, S., Bowen, W.P.: Waveguide-integrated chip-scale optomechanical magnetometer. *Optics Express* **31**(23), 37663–37672 (2023)
- [34] Shekhar, S., Bogaerts, W., Chrostowski, L., Bowers, J.E., Hochberg, M., Soref, R., Shastri, B.J.: Roadmapping the next generation of silicon photonics. *Nature Communications* **15**(1), 751 (2024)
- [35] Atabaki, A.H., Moazeni, S., Pavanello, F., Gevorgyan, H., Notaros, J., Alloatti, L., Wade, M.T., Sun, C., Kruger, S.A., Meng, H., *et al.*: Integrating photonics with silicon nanoelectronics for the next generation of systems on a chip. *Nature* **556**(7701), 349–354 (2018)
- [36] Dai, H., Shi, S., Yang, L., Guo, C., Chen, X.: Recent progress on the corrosion behavior of metallic materials in hf solution. *Corrosion Reviews* **39**(4), 313–337 (2021)
- [37] Ramasamy, M., Liang, C., Prorok, B.: Magneto-mechanical mems sensors for bio-detection. In: *MEMS and Nanotechnology, Volume 2: Proceedings of the 2010 Annual Conference on Experimental and Applied Mechanics*, pp. 9–15 (2011). Springer
- [38] Herrera-May, A.L., Soler-Balcazar, J.C., Vázquez-Leal, H., Martínez-Castillo, J.,

- Vigueras-Zuñiga, M.O., Aguilera-Cortés, L.A.: Recent advances of MEMS resonators for Lorentz force based magnetic field sensors: design, applications and challenges. *Sensors* **16**(9), 1359 (2016)
- [39] Luo, B., Will-Cole, A., Dong, C., He, Y., Liu, X., Lin, H., Huang, R., Shi, X., McConney, M., Page, M., *et al.*: Magnetolectric microelectromechanical and nanoelectromechanical systems for the iot. *Nature Reviews Electrical Engineering* **1**(5), 317–334 (2024)
- [40] Dreher, L., Weiler, M., Pernpeintner, M., Huebl, H., Gross, R., Brandt, M.S., Goennenwein, S.T.: Surface acoustic wave driven ferromagnetic resonance in nickel thin films: Theory and experiment. *Physical Review B—Condensed Matter and Materials Physics* **86**(13), 134415 (2012)
- [41] Tereshchenko, O., Bakin, V., Stepanov, S., Golyashov, V., Mikaeva, A., Kustov, D., Rusetsky, V., Rozhkov, S., Scheibler, H., Demin, A.Y.: Direct spin-imaging detector based on freestanding magnetic nanomembranes. *Physical Review Letters* **134**(15), 157002 (2025)
- [42] Liu, Z., Liang, Z., Tang, W., Xu, X.: Design and fabrication of low-deformation micro-bolometers for thz detectors. *Infrared Physics & Technology* **105**, 103241 (2020)
- [43] Dao, T.D., Doan, A.T., Ishii, S., Yokoyama, T., Ørjan, H.S., Ngo, D.H., Ohki, T., Ohi, A., Wada, Y., Niikura, C., *et al.*: MEMS-based wavelength-selective bolometers. *Micromachines* **10**(6), 416 (2019)
- [44] Pirkkalainen, J.-M., Cho, S., Li, J., Paraoanu, G., Hakonen, P., Sillanpää, M.: Hybrid circuit cavity quantum electrodynamics with a micromechanical resonator. *Nature* **494**(7436), 211–215 (2013)
- [45] O’Connell, A.D., Hofheinz, M., Ansmann, M., Bialczak, R.C., Lenander, M., Lucero, E., Neeley, M., Sank, D., Wang, H., Weides, M., *et al.*: Quantum ground state and single-phonon control of a mechanical resonator. *Nature* **464**(7289), 697–703 (2010)
- [46] Armani, D., Kippenberg, T., Spillane, S., Vahala, K.: Ultra-high-Q toroid microcavity on a chip. *Nature* **421**(6926), 925–928 (2003)
- [47] Lee, H., Chen, T., Li, J., Yang, K.Y., Jeon, S., Painter, O., Vahala, K.J.: Chemically etched ultrahigh-Q wedge-resonator on a silicon chip. *Nature Photonics* **6**(6), 369–373 (2012)
- [48] Yang, K.Y., Oh, D.Y., Lee, S.H., Yang, Q.-F., Yi, X., Shen, B., Wang, H., Vahala, K.: Bridging ultrahigh-Q devices and photonic circuits. *Nature Photonics* **12**(5), 297–302 (2018)

- [49] Bekker, C., Baker, C.G., Kalra, R., Cheng, H.-H., Li, B.-B., Prakash, V., Bowen, W.P.: Free spectral range electrical tuning of a high quality on-chip microcavity. *Optics Express* **26**(26), 33649–33670 (2018)
- [50] Su, Y., He, Y., Guo, X., Xie, W., Ji, X., Wang, H., Cai, X., Tong, L., Yu, S.: Scalability of large-scale photonic integrated circuits. *ACS Photonics* **10**(7), 2020–2030 (2023)
- [51] Eichenfield, M., Camacho, R., Chan, J., Vahala, K.J., Painter, O.: A picogram- and nanometre-scale photonic-crystal optomechanical cavity. *Nature* **459**(7246), 550–555 (2009)
- [52] Winger, M., Blasius, T.D., Alegre, T.P.M., Safavi-Naeini, A.H., Meenehan, S., Cohen, J., Stobbe, S., Painter, O.: A chip-scale integrated cavity-electro-optomechanics platform. *Opt. Express* **19**(25), 24905–24921 (2011)
- [53] Engelsen, N.J., Beccari, A., Kippenberg, T.J.: Ultrahigh-quality-factor micro- and nanomechanical resonators using dissipation dilution. *Nature Nanotechnology* **19**(6), 725–737 (2024)
- [54] Sementilli, L., Romero, E., Bowen, W.P.: Nanomechanical dissipation and strain engineering. *Advanced Functional Materials* **32**(3), 2105247 (2022)
- [55] Ghadimi, A.H., Fedorov, S.A., Engelsen, N.J., Beryhi, M.J., Schilling, R., Wilson, D.J., Kippenberg, T.J.: Elastic strain engineering for ultralow mechanical dissipation. *Science* **360**(6390), 764–768 (2018)
- [56] Fedorov, S.A., Engelsen, N.J., Ghadimi, A.H., Beryhi, M.J., Schilling, R., Wilson, D.J., Kippenberg, T.J.: Generalized dissipation dilution in strained mechanical resonators. *Physical Review B* **99**(5), 054107 (2019)
- [57] Tsaturyan, Y., Barg, A., Polzik, E.S., Schliesser, A.: Ultracoherent nanomechanical resonators via soft clamping and dissipation dilution. *Nature nanotechnology* **12**(8), 776–783 (2017)
- [58] Beryhi, M.J., Beccari, A., Groth, R., Fedorov, S.A., Arabmoheghi, A., Kippenberg, T.J., Engelsen, N.J.: Hierarchical tensile structures with ultralow mechanical dissipation. *Nature Communications* **13**(1), 3097 (2022)
- [59] Beccari, A., Visani, D.A., Fedorov, S.A., Beryhi, M.J., Boureau, V., Engelsen, N.J., Kippenberg, T.J.: Strained crystalline nanomechanical resonators with quality factors above 10 billion. *Nature Physics* **18**(4), 436–441 (2022)
- [60] Sun, C., Wade, M.T., Lee, Y., Orcutt, J.S., Alloatti, L., Georgas, M.S., Waterman, A.S., Shainline, J.M., Avizienis, R.R., Lin, S., *et al.*: Single-chip microprocessor that communicates directly using light. *Nature* **528**(7583), 534–538 (2015)

- [61] Stojanović, V., Ram, R.J., Popović, M., Lin, S., Moazeni, S., Wade, M., Sun, C., Alloatti, L., Atabaki, A., Pavanello, F., *et al.*: Monolithic silicon-photonics platforms in state-of-the-art CMOS SOI processes. *Optics Express* **26**(10), 13106–13121 (2018)
- [62] Lee, Y.-I., Park, K.-H., Lee, J., Lee, C.-S., Yoo, H.J., Kim, C.-J., Yoon, Y.-S.: Dry release for surface micromachining with HF vapor-phase etching. *Journal of microelectromechanical systems* **6**(3), 226–233 (1997)
- [63] Nivedita, L.R., Manivel, P., Pandian, R., Murugesan, S., Morley, N.A., Asokan, K., Rajendra Kumar, R.T.: Enhancement of magnetostrictive properties of galfenol thin films. *J. Magn. Magn. Mater.* **451**, 300–304 (2018)
- [64] Adolphi, B., McCord, J., Bertram, M., Oertel, C., Merkel, U., Marschner, U., Schäfer, R., Wenzel, C., Fischer, W.: Improvement of sputtered galfenol thin films for sensor applications. *Smart materials and structures* **19**(5), 055013 (2010)
- [65] Greenall, H., Carey, B.J., Bulla, D., Gotardo, F., Harris, G.I., Bennett, J.S., Foster, S., Bowen, W.P.: Quantitative profilometric measurement of magnetostriction in thin-films. *Applied Surface Science* **662**, 160105 (2024)
- [66] Ilgaz, F., Spetzler, E., Wiegand, P., Faupel, F., Rieger, R., McCord, J., Spetzler, B.: Miniaturized double-wing ΔE -effect magnetic field sensors. *Scientific Reports* **14**(1), 11075 (2024)
- [67] Shi, J., Wu, M., Hu, W., Lu, C., Mu, X., Zhu, J.: A study of high piezomagnetic (Fe-Ga/Fe-Ni) multilayers for magnetoelectric device. *Journal of Alloys and Compounds* **806**, 1465–1468 (2019)
- [68] García-Arribas, A.: In: Franco, V., Dodrill, B. (eds.) *Magnetostrictive Materials*, pp. 727–750. Springer, Cham (2021)
- [69] Wasserman, W., Harrison, R., Harris, G., Sawadsky, A., Sfindla, Y., Bowen, W., Baker, C.: Cryogenic and hermetically sealed packaging of photonic chips for optomechanics. *Optics Express* **30**(17), 30822–30831 (2022)
- [70] Velha, P., Picard, E., Charvolin, T., Hadji, E., Rodier, J.-C., Lalanne, P., Peyrade, D.: Ultra-high Q/V Fabry-Perot microcavity on SOI substrate. *Optics Express* **15**(24), 16090–16096 (2007)
- [71] Almeida, V.R., Xu, Q., Barrios, C.A., Lipson, M.: Guiding and confining light in void nanostructure. *Optics letters* **29**(11), 1209–1211 (2004)
- [72] Navarathna, A., Carey, B.J., Bennett, J.S., Khademi, S., Bowen, W.P.: Silicon double-disk optomechanical resonators from wafer-scale double-layered silicon-on-insulator. *Optics Express* **32**(23), 41376–41389 (2024)

- [73] Xia, J., Qiao, Q., Zhou, G., Chau, F.S., Zhou, G.: Opto-mechanical photonic crystal cavities for sensing application. *Applied Sciences* **10**(20) (2020)
- [74] Woolf, D., Hui, P.-C., Iwase, E., Khan, M., Rodriguez, A.W., Deotare, P., Bulu, I., Johnson, S.G., Capasso, F., Loncar, M.: Optomechanical and photothermal interactions in suspended photonic crystal membranes. *Optics Express* **21**(6), 7258–7275 (2013)
- [75] Tiecke, T., Nayak, K., Thompson, J.D., Peyronel, T., Leon, N.P., Vuletić, V., Lukin, M.: Efficient fiber-optical interface for nanophotonic devices. *Optica* **2**(2), 70–75 (2015)
- [76] McQueen, L.R., Bawden, N., Carey, B.J., Marinković, I., Bowen, W.P., Harris, G.I.: Fibre-coupled photonic crystal hydrophone. *Optics Express* **33**(12), 25910–25921 (2025)
- [77] Xu, P., Yao, K., Zheng, J., Guan, X., Shi, Y.: Slotted photonic crystal nanobeam cavity with parabolic modulated width stack for refractive index sensing. *Optics Express* **21**(22), 26908–26913 (2013)
- [78] Leijssen, R., Verhagen, E.: Strong optomechanical interactions in a sliced photonic crystal nanobeam. *Scientific reports* **5**(1), 15974 (2015)
- [79] Wang, C., Quan, Q., Kita, S., Li, Y., Lončar, M.: Single-nanoparticle detection with slot-mode photonic crystal cavities. *Applied Physics Letters* **106**(26) (2015)
- [80] Sparks, D.R., Massoud-Ansari, S., Najafi, N.: Chip-level vacuum packaging of micromachines using nanogetters. *IEEE Transactions on Advanced Packaging* **26**(3), 277–282 (2003)
- [81] Wang, H., Yin, B., Bai, J., Wei, X., Huang, W., Chang, Q., Jia, H., Chen, R., Zhai, Y., Wu, Y., *et al.*: Giant magneto-photoluminescence at ultralow field in organic microcrystal arrays for on-chip optical magnetometer. *Nature Communications* **15**(1), 3995 (2024)
- [82] Hoese, M., Koch, M.K., Bharadwaj, V., Lang, J., Hadden, J.P., Yoshizaki, R., Giakoumaki, A.N., Ramponi, R., Jelezko, F., Eaton, S.M., *et al.*: Integrated magnetometry platform with stackable waveguide-assisted detection channels for sensing arrays. *Physical Review Applied* **15**(5), 054059 (2021)
- [83] Zhang, J., Nuño-Ruano, P., Le Roux, X., Cassan, E., Marris-Morini, D., Vivien, L., Lanzillotti-Kimura, N.D., Ramos, C.: Optomechanical cavities in silicon-on-insulator. In: *Integrated Optics: Devices, Materials, and Technologies XXVII*, vol. 12424, pp. 12–16 (2023). SPIE
- [84] Nelson, A.M., Sanjuan, J., Guzmán, F.: 1/f noise mitigation in an opto-mechanical sensor with a Fabry–Pérot interferometer. *Sensors* **24**(6), 1969

(2024)

- [85] Yu, Y., Forstner, S., Rubinsztein-Dunlop, H., Bowen, W.P.: Modelling of cavity optomechanical magnetometers. *Sensors* **18**(5) (2018)
- [86] Enzian, G., Wang, Z., Simonsen, A., Mathiassen, J., Vibel, T., Tsaturyan, Y., Tagantsev, A., Schliesser, A., Polzik, E.S.: Phononically shielded photonic-crystal mirror membranes for cavity quantum optomechanics. *Optics Express* **31**(8), 13040–13052 (2023)
- [87] Kraft, F.A., Harwardt, K., Schardt, J., Nowotka, D., Gerken, M.: Suppressing the mechanochromism of flexible photonic crystals. *Optics Express* **31**(4), 6281–6295 (2023)
- [88] Dong, C., Li, M., Liang, X., Chen, H., Zhou, H., Wang, X., Gao, Y., McConney, M.E., Jones, J.G., Brown, G.J., et al.: Characterization of magnetomechanical properties in FeGaB thin films. *Applied Physics Letters* **113**(26) (2018)